Title	Engineering the Palladium–WSe2 interface chemistry for field effect transistors with high-performance hole contacts
Authors	Smyth, Christopher M.;Walsh, Lee A.;Bolshakov, Pavel;Catalano, Massimo;Addou, Rafik;Wang, Luhua;Kim, Jiyoung;Kim, Moon J.;Young, Chadwin D.;Hinkle, Christopher L.;Wallace, Robert M.
Publication date	2018-12-07
Original Citation	Smyth, C. M., Walsh, L. A., Bolshakov, P., Catalano, M., Addou, R., Wang, L., Kim, J., Kim, M. J., Young, C. D., Hinkle, C. L. and Wallace, R. M. (2018) 'Engineering the Palladium–WSe2 interface chemistry for field effect transistors with high-performance hole contacts', ACS Applied Nano Materials. doi: 10.1021/acsanm.8b01708
Type of publication	Article (peer-reviewed)
Link to publisher's version	10.1021/acsanm.8b01708
Rights	© 2018, American Chemical Society. This document is the Accepted Manuscript version of a Published Work that appeared in final form in ACS Applied Nano Materials after technical editing by the publisher. To access the final edited and published work see https://pubs.acs.org/doi/abs/10.1021/acsanm.8b01708
Download date	2024-05-06 15:00:16
Item downloaded from	https://hdl.handle.net/10468/7282

Supporting Information:

Engineering the Palladium–WSe_2 Interface Chemistry for Field Effect Transistors with High Performance Hole Contacts

Authors: Christopher M. Smyth,[†] Lee A. Walsh, [†,1] Pavel Bolshakov, [†] Massimo Catalano,[§,†] Rafik Addou,[†] Luhua Wang,[†] Jiyoung Kim,[†] Moon J. Kim,[†] Chadwin D. Young,[†] Christopher L. Hinkle,[†] Robert M. Wallace*,[†]

[†]Department of Materials Science and Engineering, University of Texas at Dallas, Richardson, Texas, 75080, USA

[§]CNR IMM, Institute for Microelectronics and Microsystems, Via Monteroni, I-73100 Lecce, Italy

*Correspondence to: rmwallace@utdallas.edu

[1] Current Address: Tyndall National Institute, Lee Maltings Complex, Dyke Parade, Cork, Ireland T12R5CP

Outline:

1. van der Waals Pd–WSe_2 Interface at Room Temperature: XPS results
2. Stoichiometry Calculation Method
3. Chemical Stability of Bulk WSe_2 Films from Room Temperature to 450 °C
4. Pd–WSe_2: Chemical State Evolution Throughout Stepwise Pd Deposition and Post Metallization Annealing under UHV Conditions
5. Pd–WSe_2: Chemical State Evolution Throughout Post Metallization Annealing under FG Conditions
6. Bond Dissociation Energies Relevant to the Pd–WSe_2 System in the Presence of Forming Gas
7. Raman Laser–Induced Damage in WSe_2 Flakes and Optimizing Parameters to Prevent Damage
8. Oxygen in Pd–Few Layer WSe_2 Structures According to EDS
9. Constructing Band Diagrams from the Valence Band Edge, Secondary Electron Cutoff, and WSe_2 Core Level Shifts
10. Mono & Few Layer WSe_2 Flakes: Pre–Metallization AFM Images and Raman Spectra
11. Determining Critical Thickness of Pd on WSe_2 as well as Si on Pd for Pinhole–Free Films
12. Nonlinear Arrhenius Plots from Pd–WSe_2 Schottky Diodes
13. Extracting Schottky Barrier Height and Unintentional Doping Density from Pd–WSe_2 Schottky Diodes
14. Analytical Schottky Barrier Height Model using Landauer Transport Theory
15. Transfer Characteristics of Back Gated WSe_2 Transistors

1. van der Waals Pd–WSe_2 Interface at Room Temperature: XPS Results

When deposited at room temperature (RT), reaction products are not detected at the Pd–WSe_2 interface regardless of chamber pressure. The chemical states detected in the corresponding Se 3*d*, W 4*f*, and Pd 3*d* core level spectra reflect bulk WSe_2 and metallic Pd, respectively (Figure S1a). The WSe_2 chemical states in the W 4*f* and Se 3*d* core level spectra shift to lower binding energy (BE) after Pd deposition under either UHV or HV conditions indicating the E_F shifts towards the valence band edge. This is consistent with upward band bending in WSe_2 due to the high Φ of Pd relative to the E_F of WSe_2.

The two spin orbit split branches of the Pd 3*d* core level spectrum detected following Pd deposition on WSe_2 in UHV exhibit larger full widths at half maximum (FWHM) than that of the metal Pd 3*d* reference spectrum (Figure S1b). However, the BE of the Pd $3d_{5/2}$ core level obtained following deposition under UHV and HV conditions (Pd^0: 334.96 eV) agrees well with that of the Pd reference film obtained in this work (334.93 eV). Furthermore, Pd 3*d* core level peak shapes similar to those obtained after Pd deposition at RT in this work have been observed previously in photoemission studies of Pd films on MoS_2[1] and isolated Pd clusters on various substrates.[2] It is also noted that any oxygen based species present on the 'initial' exfoliated WSe_2 samples employed in this work are below the limit of XPS detection (Figure S1c). The Pd $3p_{3/2}$ and O 1*s* core levels, when carefully deconvolved, indicates that oxygen is below the limit of detection after Pd deposition in UHV (Figure S1c). This deconvolution/fitting procedure is discussed in greater detail later in this section. Both the reference metal Pd film and the Pd deposited on WSe_2 in UHV exhibit asymmetric line shapes consistent with core hole screening in metallic species.[3] However, the two spin orbit split peaks in the 'UHV' Pd 3*d* spectrum are slightly more asymmetric than that of the reference Pd film, which is assumed to be an inherent feature of the Pd islands comprising

the film deposited on WSe_2 and not due to Pd–O formation. Therefore, only metallic Pd is detected when Pd is deposited on WSe_2 at RT in UHV in contrast to the pronounced Pd–C chemical state detected in the Pd 3*d* core level spectrum from the Pd–graphite interface.[4]

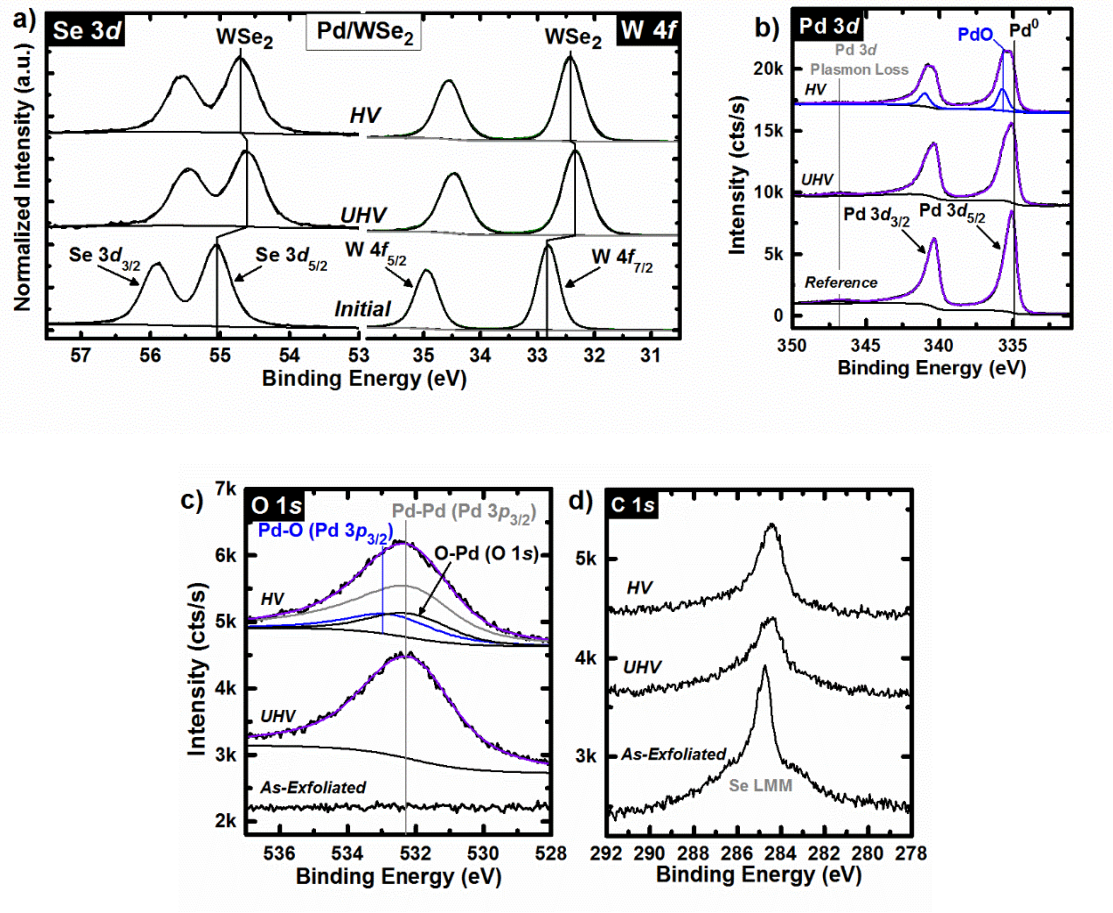

Figure S1: a) Se 3*d*, W 4*f*, b) Pd 3*d*, c) O 1*s* and d) C 1*s* core level spectra obtained by XPS from exfoliated WSe_2 (Initial) and following Pd deposition under UHV and HV conditions.

Oxygen is below the limit of XPS detection on exfoliated WSe_2. The broad peak detected in the same region as the O 1*s* core level after Pd deposition in UHV corresponds with the Pd $3p_{3/2}$ core level. The Pd $3p_{3/2}$ and O 1*s* core levels are deconvolved by applying fitting parameters obtained from the reference Pd $3p_{3/2}$ and Pd $3d_{5/2}$ core level spectra (Pd $3p_{3/2}$ full width at half maximum and double lorentzian factor = 2.85 eV and 1.6, respectively; separation between Pd $3p_{3/2}$ and Pd $3d_{5/2}$ core levels = 197.00 eV). Any additional chemical states necessary to obtain an

accurate fit ($\chi^2 \leq 0.001$) of the raw data are attributed to the O 1*s* core level. Applying the reference fit parameters to the peak in the 'UHV' spectrum in Figure S1a yields an accurate fit of the raw data, which indicates oxygen is below the limit of XPS detection (<0.1 at. %) after Pd deposition in UHV. When deconvoluting the 'HV' spectrum in Figure S1a, two chemical states with 0.72 eV separation and 0.34 area ratio (Pd–O:Pd–Pd ratio, obtained from the two chemical states fit to the corresponding Pd 3*d* spectrum) are employed to fit the Pd $3p_{3/2}$ contribution to the overall spectrum. An additional peak is included to obtain an accurate fit of the raw data, which is assigned to the O–Pd chemical state in the O 1*s* core level.

The spectra shown in Figure S1b are convoluted by the C 1*s* core level (narrow peak) and a broad Se LMM Auger peak. A chemical state corresponding with adventitious carbon is detected in the C 1*s* spectrum obtained from exfoliated WSe_2 (~284.6 eV) and shifts ~0.4 eV to lower binding energy (BE) after Pd is deposited (independent of deposition chamber base pressure). The bulk WSe_2 chemical states in the W 4*f* and Se 3*d* core levels also shift ~0.4 eV to lower binding energy, which indicates band bending induced in the WSe_2 by the deposited Pd also manifests as a E_F shift in the adventitious carbon. The chemical state in the C 1*s* core level associated with C–Pd bonds at Pd/graphene and Pd/graphite interfaces is detected at 284.0 eV,[4] which is more than 0.2 eV lower than the BE of the C 1*s* chemical state detected in this work after Pd deposition on WSe_2 substantiating our argument that Pd does not react with adventitious carbon on WSe_2.

2. Stoichiometry Calculation Method

The stoichiometry of bulk WSe_2 and any other reaction products referred to in the main text were calculated using appropriate relative sensitivity factors for the W 4*f*, Se 3*d*, and Pd 3*d*

core levels (2.959, 0.722, and 4.642, respectively, with all three reflecting both spin orbit split peaks in each of the aforementioned core levels).[5] These relative sensitivity factors apply to the particular XPS instrument employed in this study. Dividing the integrated intensity of core level spectra corresponding with the elements in a compound by these sensitivity factors permits estimation of stoichiometry and overall elemental concentration. Stoichiometry ratios calculated employing the above described method are accompanied by a ±0.2 error. For instance, intrinsic WSe_2 would exhibit a Se:W ratio of 2:1±0.2.

3. Chemical Stability of Bulk WSe_2 Films from Room Temperature to 450 °C

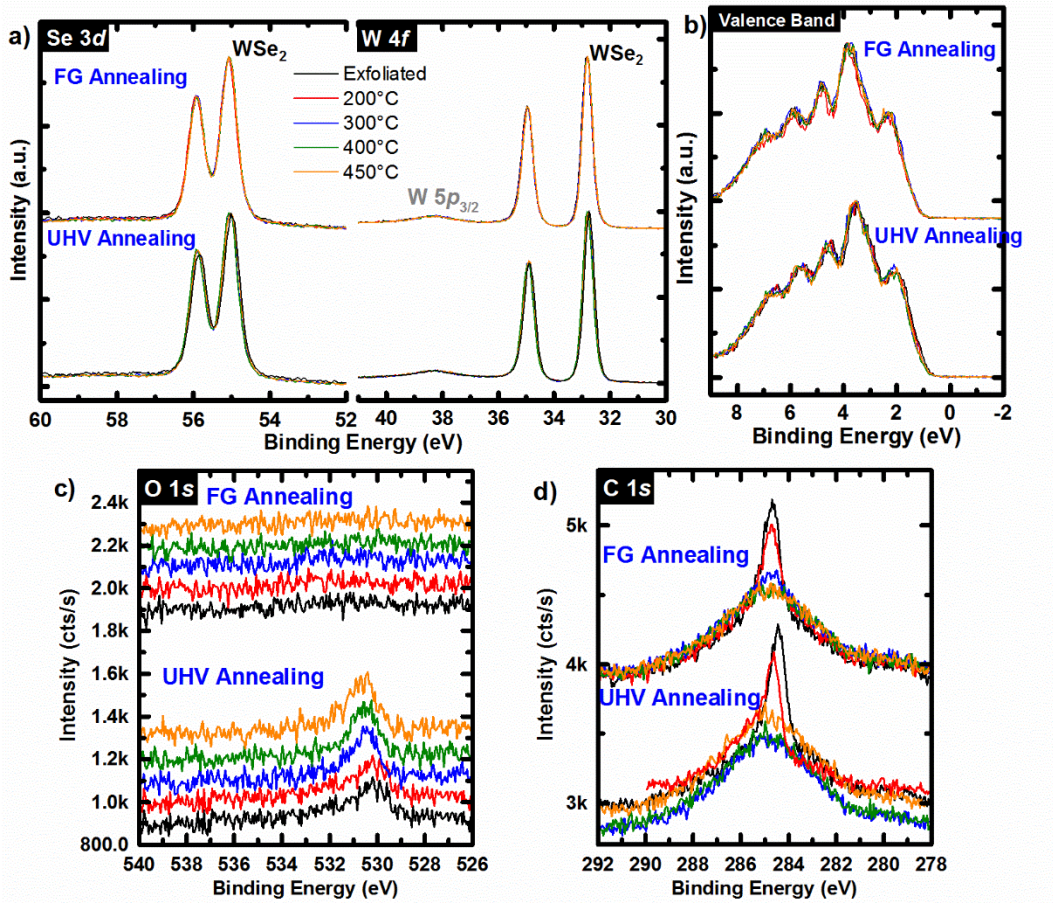

Figure S2. a) Se 3*d*, W 4*f*, b) valence band, c) O 1*s*, and d) C 1*s* core level spectra obtained throughout annealing bulk WSe_2 under UHV or FG conditions. Colors represent the anneal temperature.

The family of transition metal dichalcogenides materials are prone to defect formation (*i.e.* chalcogen vacancies) at elevated temperatures,[6,7] with increasing instability as the chalcogen atomic mass increases. Reactions between metal and TMD are likely far more favorable at defect sites within the vicinity of the TMD surface than across a defect–free van der Waals plane. Therefore, it is possible that annealing under UHV or FG conditions decomposes WSe_2 thereby facilitating reactions with Pd. Separate bulk WSe_2 samples were consecutively annealed at 200 °C, 300 °C, 400 °C, and 450 °C for one hour each under UHV or FG conditions obtaining XPS *in–situ*

after each annealing step to investigate its thermal stability at annealing temperatures employed in this work (Figure S2).

Both exfoliated WSe_2 samples exhibit sharp, symmetric doublets in the Se 3*d* and W 4*f* core level spectra consistent with a lack of E_F variation across either XPS sampling area (Figure S2a). The FWHM and binding energies of the bulk WSe_2 chemical states and also the valence band edge (Figure S2b) remain constant at all annealing temperatures and ambients, which indicates chemical stability. A small concentration of oxygen is detected on the sample annealed in UHV (Figure S2c), which likely corresponds with WO_x according to the BE at ~530.2 eV consistent with a transition metal oxide. However, this does not cause a discrepancy in the E_F between the two samples as the valence band edges detected from each sample throughout annealing align quite closely. Adventitious carbon is detected on both exfoliated WSe_2 samples, which is consistent with all bulk WSe_2 samples employed throughout this work (Figure S2d). The concentration of carbon decreases slightly while annealing at 200 °C and is completely desorbed while annealing at 300 °C regardless of annealing ambient. In addition, the Se:W ratio remains constant throughout annealing (Table S1). This provides strong evidence that bulk WSe_2 employed here is chemically stable throughout the thermal budget imparted during the annealing experiments.

Table S1: Se:W ratio calculated from core level spectra obtained from exfoliated, bulk WSe_2 prior to and throughout *in–situ* annealing under UHV (<2 × 10^{-9} mbar) and forming gas (90% N_2, 10% H_2; 1 mbar) conditions.

	Stoichiometry (Se:W)	
	UHV	FG
Exfoliated	2.01	1.99
200°C	2.01	2.07
300°C	1.99	2.06
400°C	2.00	2.04
450°C	2.00	2.01

4. Pd–WSe_2: Chemical State Evolution Throughout Stepwise Pd Deposition and Post Metallization Annealing under UHV Conditions

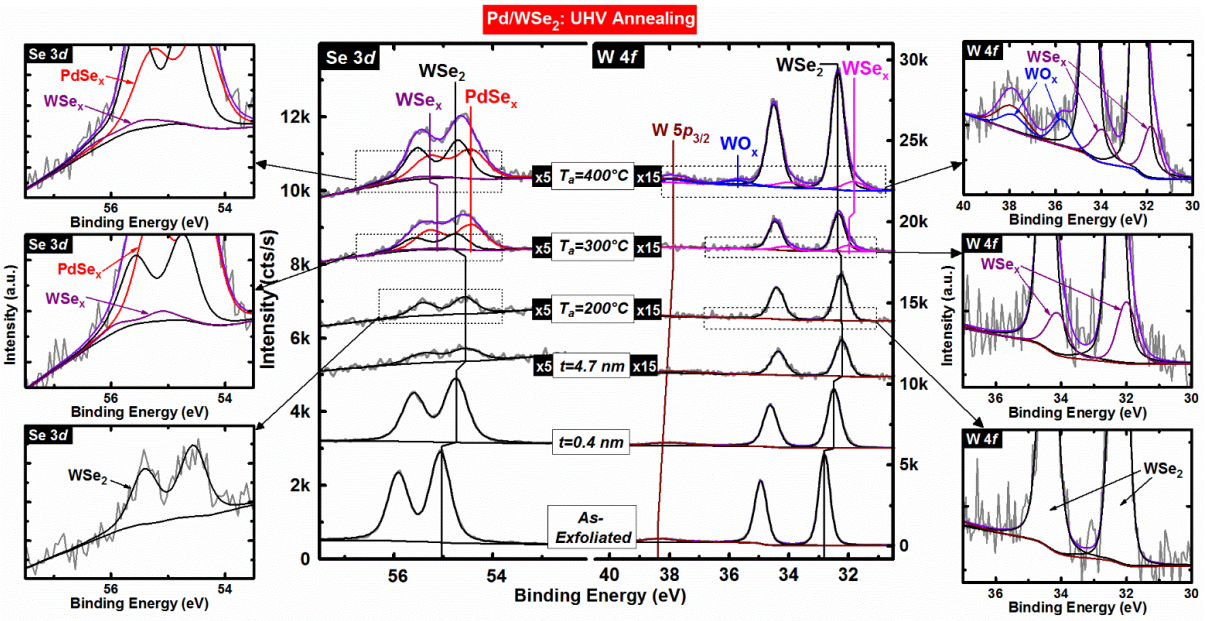

Figure S3: Deconvoluted Se 3*d*, W 4*f*, and W $5p_{3/2}$ core level spectra obtained throughout Pd deposition on WSe_2 and post metallization annealing in UHV. The inset plots at right and left display magnified Se 3*d* and W 4*f* core level spectra obtained following each anneal. Residuals associated with the peak fits are 0.001 % (not shown for clarity).

Figure S3 displays the evolution of the Se 3*d* and W 4*f* core level spectra throughout stepwise Pd deposition and post metallization annealing under UHV conditions. The chemical states in the

Se 3*d* and W 4*f* core levels are initially detected from exfoliated WSe_2 at binding energies of 55.05 and 32.80 eV, respectively, and remain the only detectable chemical states throughout Pd deposition. Expanded Se 3*d* and W 4*f* core level spectra obtained following each anneal are displayed adjacent to Figure S3 accentuating minute changes with increased annealing temperature. The formation of $PdSe_x$ after annealing at 300 °C is evidenced by the additional state appearing at low BE (54.42 eV) in the corresponding Se 3*d* core level. Concomitant formation of WSe_x is evidenced by the high BE state (55.11 eV) in the Se 3*d* core level and corresponding low BE state in the W 4*f* core level (31.99 eV). No W–W bonding is detected at 31.20 eV in the W 4*f* core level spectrum throughout the experiment. $PdSe_x$ exhibits a Se^{2-} chemical state with lower BE than that of bulk WSe_2 due to the greater electronegativity difference between Pd and Se (0.35) compared with that between W and Se (0.19).[8] This results in a greater ionic character associated with the Pd–Se bond compared with the W–Se bond in WSe_2.

The chemical states associated with WSe_x shift by +0.29 eV and -0.15 eV in the Se 3*d* and W 4*f* core level spectra, respectively, following the 400 °C UHV anneal. This suggests further WSe_x reduction with increased annealing temperature as the binding energies of the associated chemical states shift towards the expected binding energies of elemental Se (55.50 eV) and W (31.20 eV), respectively.

In addition, WO_x is detected in the W 4*f* core level after annealing at 400 °C as evidenced by the appearance of a high BE state at 35.69 eV. The Pd film undergoes mild agglomeration at 400 °C, possibly leaving regions of extremely thin Pd or even exposed WSe_x or WSe_2. WO_x formation could occur in these regions from reactions with background gases in the chamber considering the pressure increases to ~10^{-7} mbar during the first 10 minutes of the anneal, then decreases quickly into UHV.

The normalized O 1*s* core level spectra obtained after RT Pd deposition and *in–situ* annealing under UHV conditions are shown in Figure S4. The Pd $3p_{3/2}$ core level convolutes the O 1*s* core level spectrum. There are no resolvable peaks below 531.0 eV that would suggest the formation of Pd–O or W–O bonds throughout the experiment. However, the intensity of the WO_x chemical state in the W 4*f* core level spectrum obtained after 400 °C UHV anneal (Figure S3) suggests the intensity of the associated oxygen chemical state should be comparable with the noise detected in the corresponding O 1*s* core level spectrum.

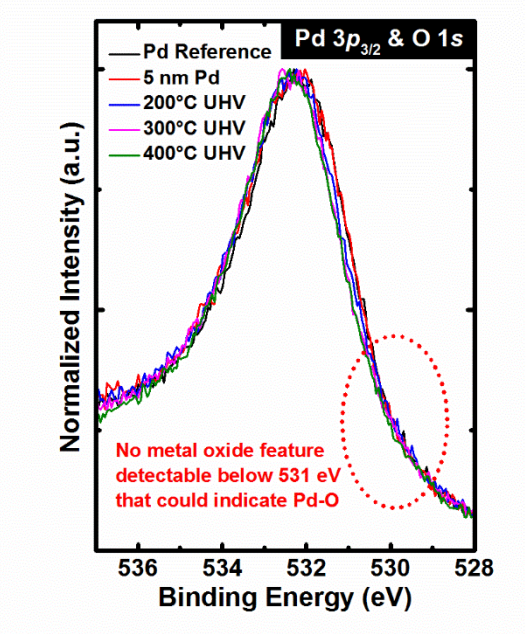

Figure S4: O 1*s* core level spectra convoluted by the Pd $3p_{3/2}$ core level spectra obtained after ~5 nm Pd deposition on WSe_2 and post metallization annealing in UHV.

5. Pd–WSe_2: Chemical State Evolution Throughout Post Metallization Annealing under FG Conditions

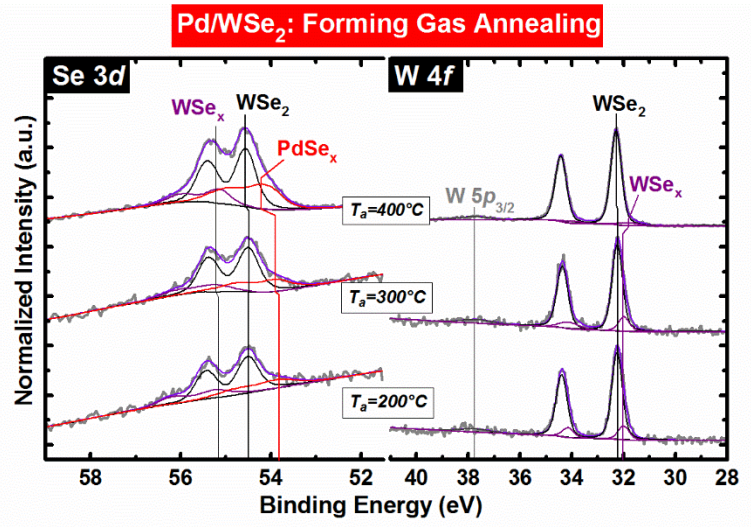

Figure S5: Deconvoluted Se 3*d*, W 4*f*, and W $5p_{3/2}$ core level spectra obtained after annealing a ~50 Å Pd–WSe_2 structure in forming gas (1 mbar) for 1 hr at 200 °C, 300 °C, and 400 °C, respectively.

Pd reduces WSe_2 and forms substoichiometric WSe_x during the 200 °C FG anneal as shown by the appearance of chemical states at 55.27 and 31.99 eV in the corresponding Se 3*d* and W 4*f* core level spectra (Figure S5) in addition to those of the bulk WSe_2. Concomitant $PdSe_x$ formation is detected at 53.86 eV in the corresponding Se 3*d* core level spectrum. However, the WSe_x chemical state in the W 4*f* (Se 3*d*) core level shifts -0.19 eV (-0.13 eV) towards elemental W (away from elemental Se) after the 400 °C FG anneal consistent with a decreased (increased) oxidation state. Considering the Pauling electronegativities of Pd (2.20) and W (2.36),[8] the BE shifts exhibited by the WSe_2 chemical states after 400 °C FG anneal suggest W–Se–Pd bonds form as an intermediate step to $PdSe_x$ formation.

Any WO_x that forms while annealing in FG remains below the limit of detection. Metallic W also remains below the limit of XPS detection throughout FG anneals.

6. Bond Dissociation Energies Relevant to the Pd–WSe_2 System in the Presence of Forming Gas

Table S2: Bond dissociation energies of relevant bonds in the Pd–WSe_2 system in the presence of FG.

	kJ/mol	kcal/mol	eV
H-H[9]	432.1	103.27	4.48
W-Se[10]	418.1	99.92	4.33
H-Se[11]	310.7	74.26	3.22
H-(SeH)[11]	330.1	78.89	3.42
H-(Se^+)[9]	306.0	73.14	3.17
H-(Se^-)[9]	331.0	79.11	3.43
H-Pd(diatomic)[9]	234.0±25.0	55.93±5.98	2.43±0.26
H-Pd(polycrystalline)[9]	59	14.10	0.61
H-Pd(111)[9]	253.0	60.47	2.62
H_2-Pd(111)[9]	87.0	20.79	0.90
Pd-Pd[9]	136.0	32.50	1.41
H-(W^+)[9]	222.5	53.18	2.31
H-W(100)[9]	283.0	67.64	2.93
H-W(110)[9]	285.0	68.12	2.95
H-W(111)[9]	294.0	70.27	3.05
H-W(211)[9]	289.0	69.07	3.00
H_2-W(polycrystalline)[9]	134.0	32.03	1.39
H_2-W(100)[9]	156.0	37.28	1.62
H_2-W(110)[9]	136.8	32.70	1.42
H_2-W(111)[9]	153.0	36.57	1.59
H_2-W(211)[9]	146.0	34.89	1.51
Pd-Se	Not known		

In the main text, some of the bond dissociation energies listed above and related Gibbs free energies of formation are employed to formulate the reaction mechanism that validates the onset of $PdSe_x$ formation at lower annealing temperature and ~3× greater $PdSe_x$ concentration after 400 °C anneal when annealing is performed in FG compared with UHV.

7. Raman Laser–Induced Damage in WSe_2 Flakes and Optimizing Parameters to Prevent Damage

Laser induced damage has been observed previously in MoS_2 due to Joule heating when great enough power density, exposure time, and/or a large enough number of spectral accumulations are employed.[12] It is therefore reasonable to expect a similar or even greater potential for laser induced damage in other TMDs with equal or lesser chemical stability compared to MoS_2, such as WSe_2.[13] Laser induced interface perturbation could result in erroneous conclusions regarding the number of WSe_2 layers consumed in reactions with an overlying contact metal. Therefore, determining parameters that 1) maximize spectral intensity after metal deposition and Si capping and 2) do not damage the underlying WSe_2 (excluding spectral changes associated with reactions that occur during deposition or post metallization annealing) is critical for accurate interpretation of associated Raman spectra. Pd–Si bonds are Raman active (vibrational modes appearing between 90 and 200 cm^{-1})[14] but expected features are below the limit of detection in all Raman spectra obtained from Si capped Pd–WSe_2 samples investigated in this work.

Various combinations of laser power density (0.49 and 3.32 $mW/\mu m^2$), exposure time (1, 2, 3, 4, 5, and 10 s), and number of spectral accumulations (5, 10, and 20) were tested on the exfoliated WSe_2 surface. The surface topography and spatial variation in composition (phase) of exfoliated few layer WSe_2 flakes is investigated prior to and following Raman spectroscopy, specifically in the vicinity of regions probed by the Raman laser. Figures S6a–f show the corresponding topographical and phase images obtained by AFM. Regions probed by Raman laser are circled in green. The parameters associated with each probed location are listed in Table S3 according to the number assigned to each location.

Bright spots appear on all WSe_2 terraces in each topographical image displayed and likely reflect the roughness of the underlying SiO_2 as the flakes investigated are single or few layer in

thickness. In Figure S6a, the topography of the probed WSe_2 flake is unaffected by laser interrogation during Raman spectroscopy, whereas significant topographical and/or phase contrast is observed in the vicinity of all other probed regions in the associated AFM images (Figures S6b–f). This indicates a laser power density of 0.49 $mA/\mu m^2$, exposure time of either 5 or 10 seconds, and accumulating 5 spectra will preserve the structural and, presumably, the chemical integrity of exfoliated WSe_2. Therefore, we also assume that the same set of parameters will provide an adequate spectral resolution from WSe_2 buried under 5 nm Pd and 10 nm Si cap as evidenced by the Raman spectra shown in the main text. All other parameter combinations result in damaged WSe_2 as is evidenced by the various unusual features observed within the circled regions of Figures S6b–f after performing Raman spectroscopy. Therefore, spectra acquired from WSe_2 flakes after 5 nm Pd deposition, post metallization annealing, and finally a 10 nm Si cap were obtained with 0.49 $mW/\mu m^2$ power density, 5 s exposure, and 5 accumulations to avoid such spurious damage effects.

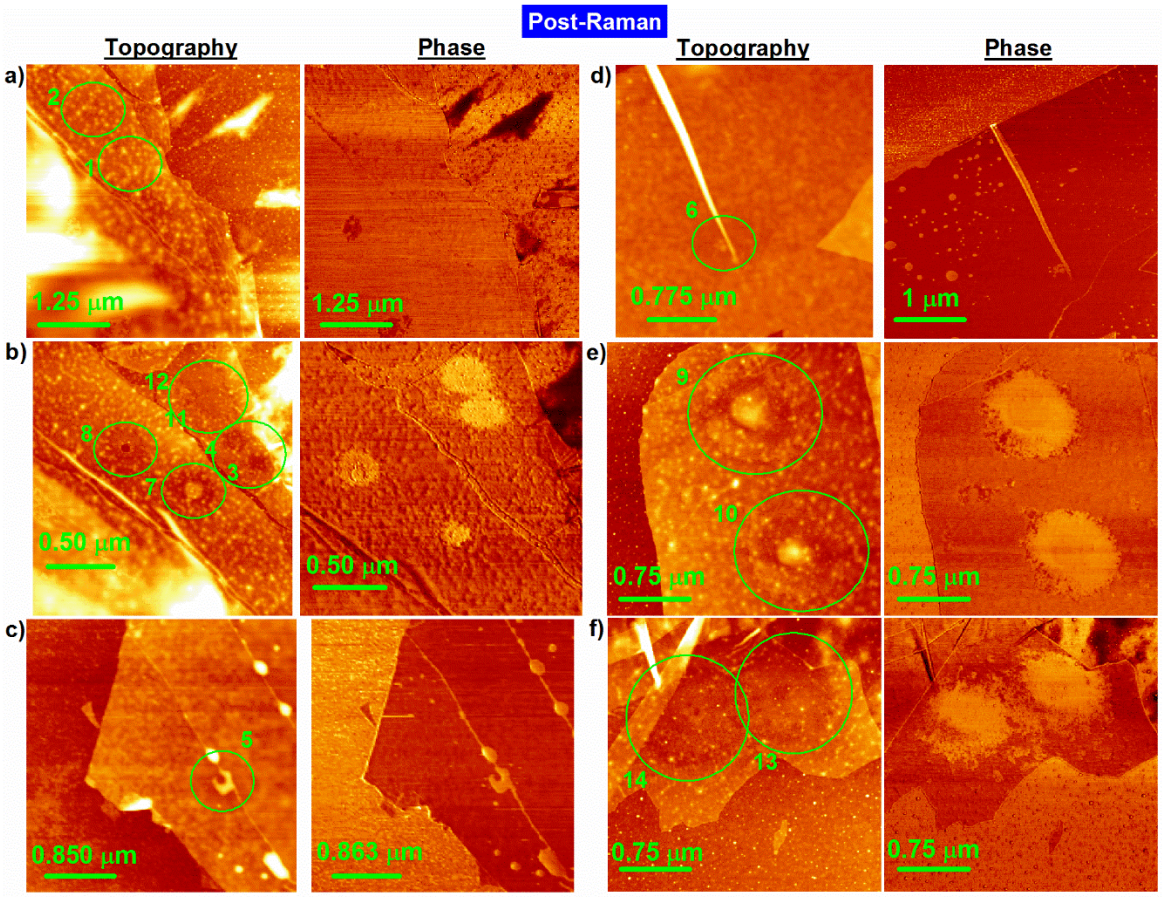

Figure S6: a-f) AFM topography and phase images obtained from exfoliated WSe_2 flakes after performing Raman spectroscopy employing a number of different parameter combinations. Each combination of parameters employed are listed according to probed location in Table S3. The green circles in each image highlight the regions probed by Raman spectroscopy. The number adjacent to each circle corresponds with the specific set of parameters employed in acquiring the associated Raman spectrum.

Table S3: Parameters employed in performing Raman spectroscopy according to probed location in each AFM image in Figure S6.

Image(spot)	Power Density ($mW/\mu m^2$)	Exposure Time (s)	Accumulations	Damage
a1	0.49	5	5	no
a2	0.49	10	5	no
b3	0.49	3	10	yes
b4	0.49	5	10	yes
b7	3.32	1	5	yes
b8	3.32	2	5	yes
b11	3.32	1	10	yes
b12	3.32	2	10	yes
c5	0.49	10	10	yes
d6	0.49	4	20	yes
e9	3.32	5	5	yes
e10	3.32	10	5	yes
f13	3.32	5	10	yes
f14	3.32	10	10	yes

It is also noted that employing a laser power density of 3.32 $mW/\mu m^2$ (and presumably anything greater than this at λ=532 nm) imparts significant damage on WSe_2 within the vicinity of the probed region regardless of parameter combination employed in this work (Table S3). The Raman spectra collected from 1L WSe_2 employing the parameters associated with b(8) in Table S3 (blue curve) as well as a spectrum from a separate 1L WSe_2 flake employing 0.49 $mW/\mu m^2$, 10 accumulations, and 1 s exposure time (black curve) are normalized according to the 2LA(M) mode and shown in Figure S7a. Both the E^1_{2g}/A_{1g} and 2LA(M) peaks obtained with parameter set 8 (blue) are redshifted by 1.5 cm^{-1} from the spectrum which was obtained without damaging WSe_2 (black). The software controlling the Raman spectrometer employed in this work sums each accumulation consecutively throughout the measurement. It is therefore possible that the redshift observed here when laser power density of 3.32 $mW/\mu m^2$ is employed manifests initially as a result of Joule heating. This is consistent with a shift to lower wavenumber (higher frequency) expected

of Raman active vibrational modes with increased temperature. The Joule heating induced by laser irradiation therefore provides enough energy to damage WSe_2 in some cases (*i.e.* Se loss and concomitant WO_x formation) and even completely evaporate WSe_2 in the case of region 8 (Figures S8a and S8b). Despite completely evaporating WSe_2 directly probed by the 3.32 $mW/\mu m^2$ laser in region 8, a Raman spectrum is still obtained. However, this is likely a result of WSe_2 evaporation occurring incrementally over the course of each accumulation, providing an appreciable signal to noise during the first few exposures. Therefore, even in severe cases where WSe_2 is completely desorbed as it appears in region 8, a Raman spectrum with reasonable signal to noise can still be obtained and other methods must be employed to test for laser induced damage.

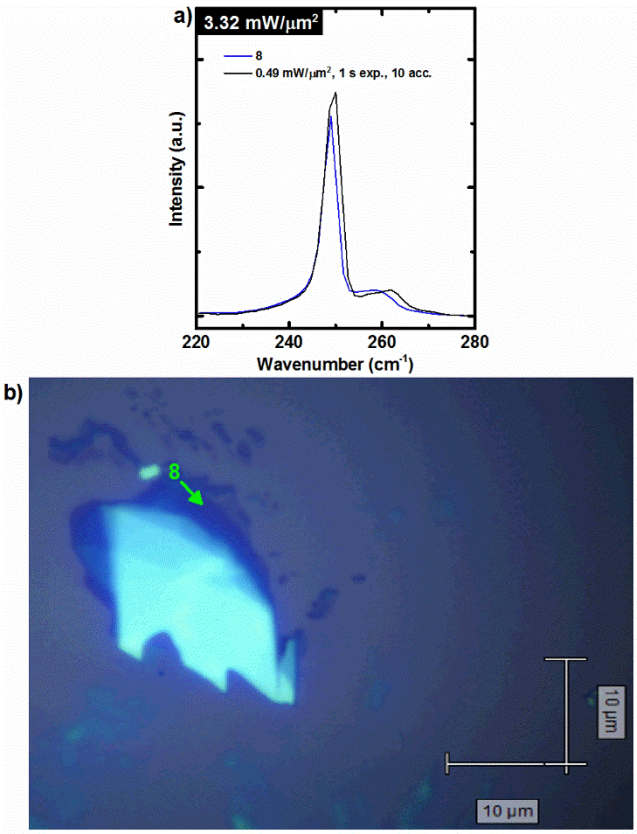

Figure S7. a) Raman spectra obtained from mono layer WSe_2 flakes with parameters according to b(8) in Table S3 (blue curve) and also with 0.49 mW/μm^2, 1 s exposure, and 10 accumulations (black curve). The spectra are normalized to the 2LA(M) mode. b) Optical microscope image of an exfoliated WSe_2 flake on SiO_2 substrate showing completely evaporated WSe_2 in region 8 (Figure S6b) as indicated by the circular feature at the end of the green arrow exhibiting a contrast nearly identical to the substrate.

8. Oxygen in Pd–Few Layer WSe_2 Structures According to EDS

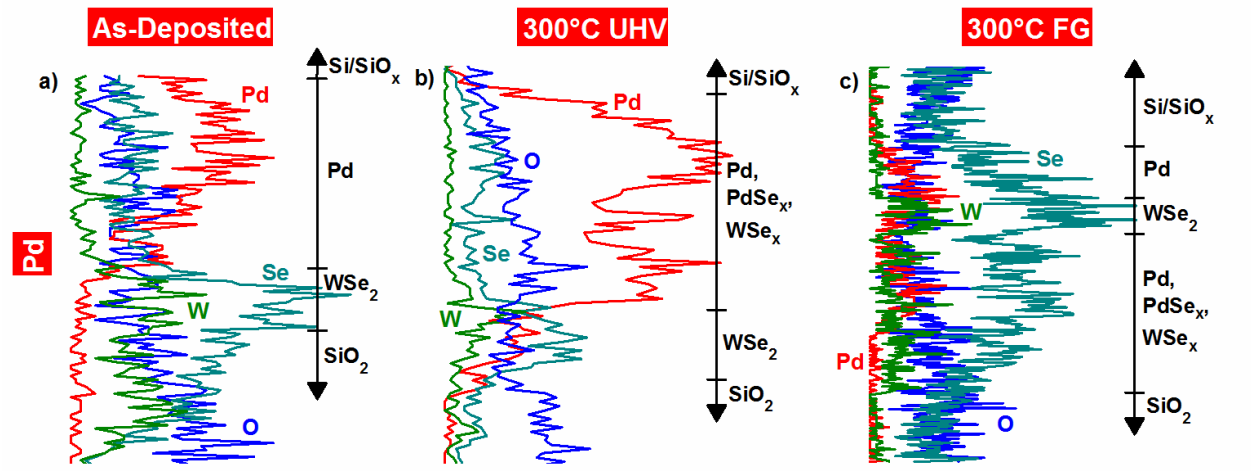

Figure S8. EDS spectra including the oxygen signal obtained from cross sections of Si/Pd/WSe_2/SiO_2 structures after a) fabrication, b) 300 °C UHV anneal, and c) 300 °C forming gas anneal.

Figure S8 shows the same EDS spectra displayed in Figures 3f–h, however the oxygen signal is included here.

9. Constructing band diagrams from Valence Band Edge, Secondary Electron Cutoff, and WSe_2 core level shifts

Figure S9 shows the valence band edges and secondary electron (SE) cutoffs obtained from all exfoliated WSe_2 according to linear regression employing a 95% confidence interval. The significance of employing a 95% confidence interval when performing linear regression is that there is a 95% probability that the extrapolated x–intercept will fall within the associated confidence interval. The confidence intervals associated with the linear regression of the 'UHV Anneal' and 'FG Anneal' SE cutoff spectra are both ±0.01 eV, while that of the 'UHV Anneal' and 'FG Anneal' valence band spectra are ±0.02 eV and ±0.03 eV, respectively. The errors displayed in Figure S9 include the ±0.05 eV error associated with the XPS measurement.

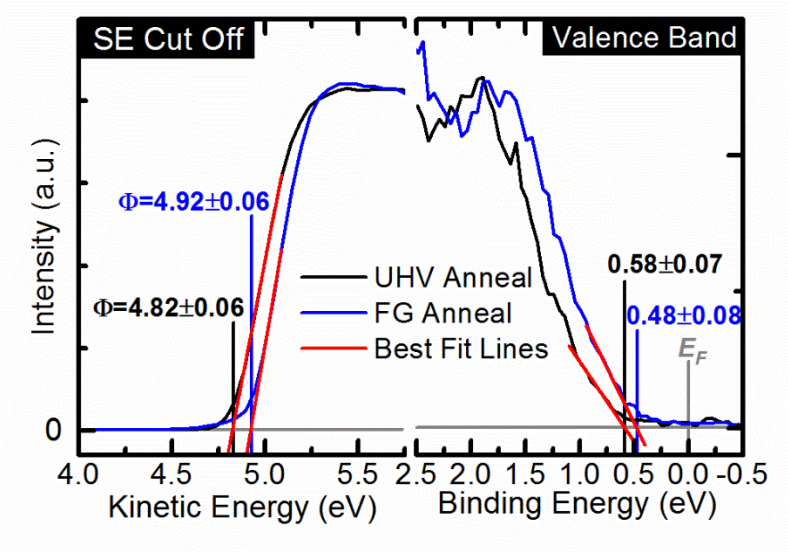

Figure S9: Secondary electron cutoff and valence band edge spectra obtained from both 'exfoliated' WSe_2 samples prior to metal deposition. The red lines show linear fits obtained by regression.

Band diagrams were constructed from a set of common relationships between valence band edge, work function, and substrate core level binding energies as follows:

$$\phi_i = E_{Ion,WSe2} - VBM_{extrapolated} \qquad \text{Eq. (1)}$$

$$\Delta\phi = \phi_i - \Delta BE_{Se\ 3d\frac{5}{2},(WSe2)} \qquad \text{Eq. (2)}$$

where Φ_i represents the initial sample work function according to the valence band offset and assumed WSe_2 ionization energy ($E_{Ion,WSe2}$; 5.4 eV),[15] $VBM_{extrapolated}$ represents the valence band offset according to the x–axis intercept obtained from linear regression, and $\Delta\Phi$ represents the change in work function after an experimental step according to the corresponding change in BE of bulk WSe_2 chemical state in the W $4f_{7/2}$ or Se $3d_{5/2}$ core level spectra ($\Delta BE_{Se\ 3d5/2(WSe2)}$). Eq. (1) from the initial, exfoliated WSe_2 surface is corroborated with the work function value obtained from the SE cutoff. A -9.82 V bias was applied to the sample with an external power source to access the SE cutoff. Bulk WSe_2 chemical state shifts to lower BE correspond with a Fermi level (E_F) shift towards the valence band edge.

Impurities and native defects inherent to bulk TMDs cause spatial E_F variability on the order of hundreds of meV.[16,17] Therefore, E_F variations across exfoliated WSe_2 prior to metal deposition observed in this work are attributed to intrinsic E_F variation rather than surface adsorbates as the concentration of adventitious carbon is similar on all exfoliated WSe_2 surfaces. Nonetheless, the E_F detected from each WSe_2 sample at room temperature after metal deposition is within the XPS detection limit of eachother. Therefore, initial E_F variability presumably does not affect the E_F after a sufficient amount of metal is deposited.

10. Single & Few Layer WSe_2 Flakes: Pre–Metallization AFM Images and Raman Spectra

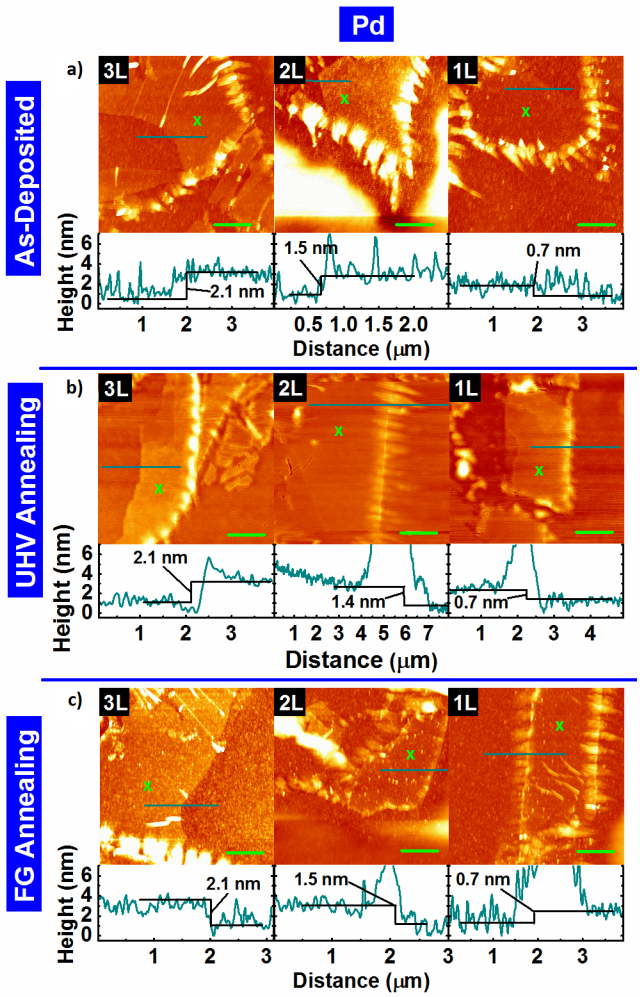

Figure S10. AFM topography images and associated line profiles of WSe_2 flakes after exfoliation and annealing. The label at the left of each row of AFM images denotes whether the flakes were subjected to a post metallization anneal after Pd deposition and before characterization by Raman spectroscopy. The green scale bar in each image represents 2 μm.

Topographic images were obtained *ex–situ* from bare WSe_2 flakes after exfoliating onto 270 nm SiO_2 substrates and annealing in N_2 at 300 °C for 1 hr to remove resist residue. A Veeco Model 3100 Dimension V Atomic Probe Microscope[18] was employed in non–contact tapping mode. Images were processed and line profiles were obtained with the WSxM software.[19]

AFM was employed in conjunction with Raman Spectroscopy to locate WSe_2 flakes with regions of one, two, and three layers. The green 'x' marked on each image in Figure S10 denotes

the region on each WSe_2 flake probed by Raman spectroscopy. The blue line in each image in Figure S10 denotes the cut represented by the line profile below each image.

11. Determining Critical Thickness of Pd on WSe_2 as well as Si cap on Pd for Pinhole–Free Films

Gong *et al.* employed Raman spectroscopy to investigate the effects of various metal films on characteristic first order vibrational modes of monolayer MoS_2.[20] However, films were not deposited to full coverage thicknesses and therefore resulted in complex, difficult to interpret Raman spectra after all metal depositions. Therefore, the minimum film thickness required for pinhole free, full coverage Pd films on WSe_2 and Si films on full coverage Pd films were determined by He^+ ion–based low energy ion scattering spectroscopy (LEISS). Pd films were deposited under UHV conditions onto exfoliated highly oriented pyrolytic graphite (HOPG), a 2D material with a van der Waals surface similar to WSe_2. Pd films were identified as pinhole free at a thickness preventing carbon detection by LEISS. Si was deposited under UHV conditions onto full coverage Pd–HOPG substrates also prepared under UHV conditions without breaking vacuum. A Si film was identified as pinhole free at a thickness preventing Pd detection by LEISS. Spectra were obtained *in–situ* immediately following metal or Si deposition without breaking vacuum. Figure S11 displays the LEISS spectra obtained from Pd films deposited on HOPG and Si films subsequently deposited on full coverage Pd.

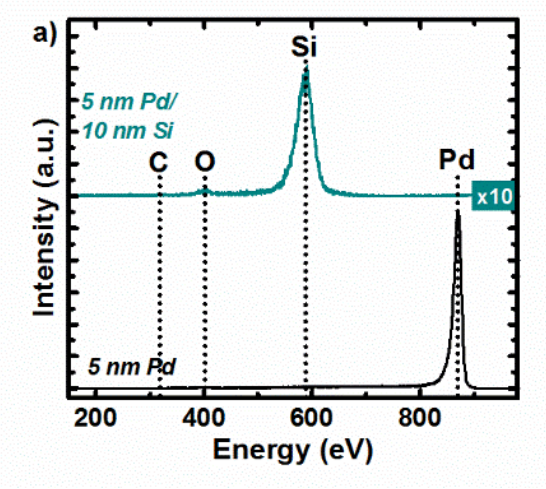

Figure S11: LEISS spectra obtained from a full coverage Pd film on HOPG and full coverage Si film on Pd.

Following 5 nm deposition of Pd on HOPG, carbon is below the limit of detection by LEISS indicating full coverage films at this thickness. 10 nm Si deposited on 5 nm of Pd prevents LEISS detection of the underlying metal indicating a full coverage, pinhole free film. Surface oxidation *in–situ* of amorphous Si evaporated by electron beam under UHV conditions is reasonable as the $\Delta G°_{SiO2}$ = -428.4 kJ/mol (per oxygen atom).[21] Therefore, oxygen detected after Si deposition is attributed to surface oxidation rather than either an incomplete Si film or oxygen incorporated throughout the Si film.

12. Nonlinear Arrhenius Plots from Pd-WSe_2 Schottky Diodes

An Arrhenius plot ($\ln(I/T^2)$ vs 1/T) of I–V data from a Schottky diode can be employed to extract the Schottky barrier height in the forward bias region for V>>kT/q, provided the transformed data can be accurately fit by linear regression. When the Arrhenius plot yields a nonlinear temperature dependence, this indicates thermionic emission does not accurately describe the transport mechanism across the diode and other mechanisms, such as tunneling or a

spatially inhomogeneous barrier height, must be considered to accurately extract the Schottky barrier height. The Arrhenius plots obtained from temperature dependent I–V measurements of Pd–WSe_2 Schottky diodes after fabrication and throughout post metallization annealing exhibit nonlinear characteristics (Figure S12), which indicates an alternative Schottky barrier height extraction method is needed to accurately determine the band alignment. After post metallization annealing at 400 °C in UHV, linear behavior is observed at 0.2 V forward bias and an electron Schottky barrier of 0.48 eV is extracted from the slope of the best fit line (Figure S12b). This barrier height is much smaller than the 'homogeneous' barrier height extracted using the inhomogeneous barrier height model (discussed in the main text), likely because the thermionic emission model considers a uniform barrier height. Therefore, the thermionic emission model will underestimate the barrier height in devices with an inhomogenenous barrier height.

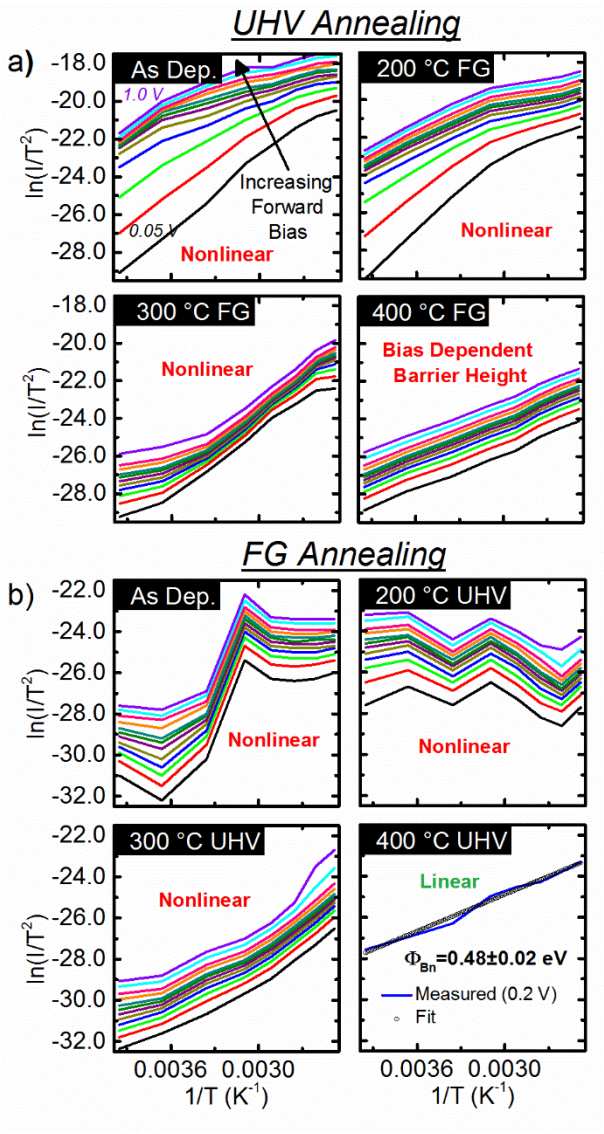

Figure S12. Arrhenius plots obtained from temperature dependent I–V measurements of Pd–bulk WSe_2 Schottky diodes after fabrication and subsequent post metallization annealing in either a) FG or b) UHV. These plots show the nonlinear behavior in all cases but one (400 °C FG), demonstrating the need for an alternative method for accurate Schottky barrier height extraction.

13. Extracting Schottky Barrier Height and Unintentional Doping Density from Pd–WSe_2 Schottky Diodes

The barrier height can vary across the metal–semiconductor interface even in mature systems such as Si and GaN, with experimentally determined low barrier height patch densities on the order of 10^7 cm^{-2}.[22] Low quality materials such as geological MoS_2 or WSe_2 have been reported to exhibit defect densities as high as 3×10^{12} cm^{-2}, which have been shown to dominate conduction across the metal–MoS_2 interface.[16,17] The inhomogeneous Schottky barrier height model[23] employed in this work to fit the forward bias I–V characteristics of Pd–WSe_2 Schottky diodes requires the doping density of the semiconductor material. This is determined by measuring the capacitance of the same Schottky diodes in reverse bias and extracting the slope (m) of the $1/C^2$ vs V plot, which is then inserted into Eq. 3 to solve for N_D-N_A,

$$m = \frac{2}{q\varepsilon_S\varepsilon_0(N_D - N_A)} \qquad \text{Eq. (3)}$$

where q is the charge of an electron, ε_S is the WSe_2 dielectric constant (7.2),[24] ε_0 is the vacuum permittivity and N_D-N_A is the unintentional doping density of the WSe_2.

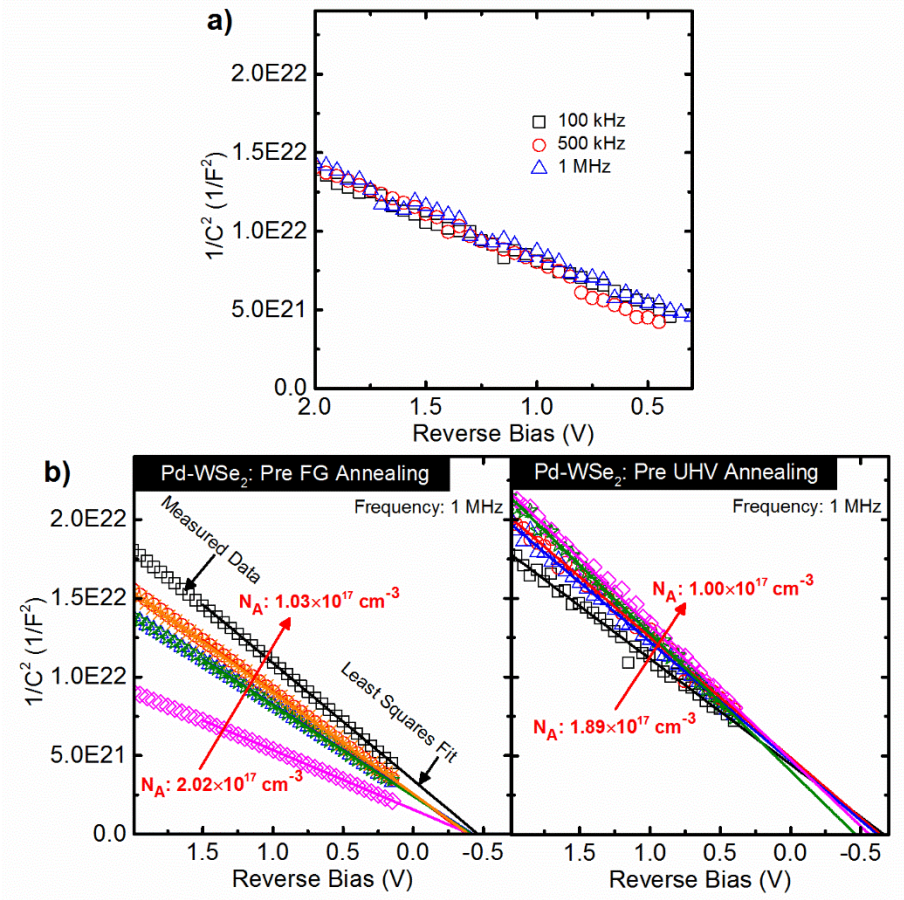

Figure S13. $1/C^2$ vs V plots and fitted lines measured from a) a Pd–WSe_2 Schottky diode demonstrating a frequency independent slope and b) from many Pd–WSe_2 Schottky diodes prior to subsequent anneals in UHV or FG (measured at 1 MHz), which demonstrate a spatially varying WSe_2 doping density across a single WSe_2 crystal and from crystal to crystal.

This method requires the data plotted as $1/C^2$ vs V to exhibit slope and intercept independent of frequency,[25] which is demonstrated in Figure S13a for three different Schottky diodes. The WSe_2 doping density varies spatially from 1.00×10^{17} cm^{-3} to 2.02×10^{17} cm^{-3}, as expected according to previous work,[16,17] according to the range of slopes fitted in the $1/C^2$ vs V plot for a number of diodes and two different synthetic WSe_2 crystals (Figures S13b).

14. Analytic Schottky Barrier Model using Landauer Transport Theory

Figure S14 shows the measured I_{DS}–V_{BG} transfer characteristics (solid lines) of two back gated WSe_2 FETs with Pd contacts after fabrication and throughout post metallization annealing in either UHV or FG. The fits of the subthreshold regions of the I_{DS}–V_{BG} curves are performed independently on each carrier branch from the point of minimum current and are also shown in Figure S14 (symbols). In–plane carrier effective masses $m_e^*=0.33m_0$ and $m_h^*=0.46m_0$ are employed in the model.[26] The transfer characteristics of the device after 300 °C FG anneal are omitted because of a measurement error. Nonetheless, the devices annealed in FG underwent consecutive anneals at 200 °C, 300 °C, and 400 °C and therefore the 400 °C FG anneal I_{DS}–V_{BG} transfer characteristics can be directly compared to those obtained from a separate device after 400 °C UHV anneal.

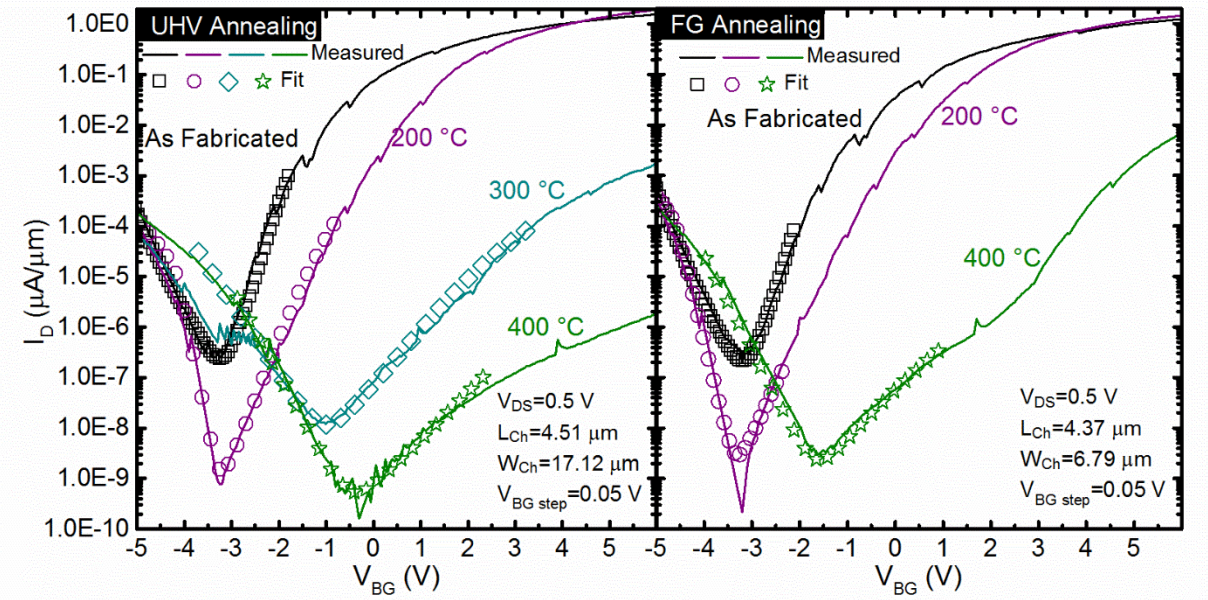

Figure S14. Measured I_{DS}–V_{BG} transfer curves from Pd–WSe_2 back gated FETs after fabrication and subsequent post metallization annealing in either UHV or FG.

15. Transfer Characteristics of Back Gated WSe_2 Transistors

Two sets of three back gated WSe_2 transistors with Pd contacts were fabricated for the study. One set was subjected to the UHV anneals and another set was subjected to the FG anneals. The corresponding transfer characteristics are shown below. Some device to device variability is measured, but this is common in TMD-based devices. The anneals reduce the device to device variability and the overall trends in Fermi level shift follows the trends reflected in Figure 6 according to device transfer characteristics.

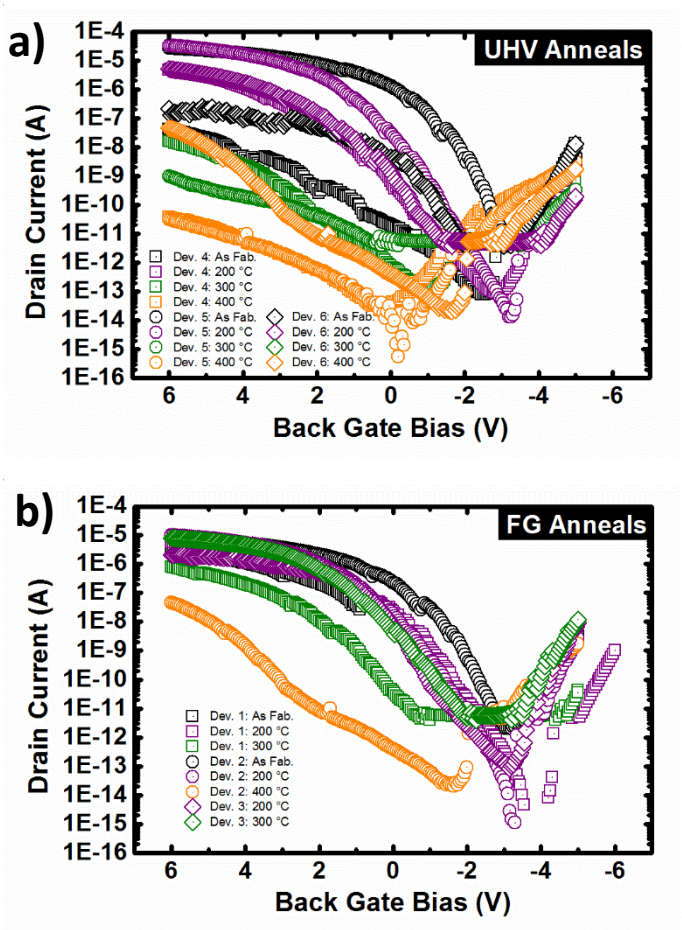

Figure S15: Measured I_{DS}–V_{BG} transfer curves from three devices annealed in a) ultra-high vacuum and b) forming gas, separately, showing agreement in the general trend and some expected device to device variability.

References:

(1) Dong, H.; Gong, C.; Addou, R.; McDonnell, S.; Azcatl, A.; Qin, X.; Wang, W.; Wang, W.-H.; Hinkle, C. L.; Wallace, R. M. Schottky Barrier Height of Pd/MoS_2 Contact by Large Area Photoemission Spectroscopy. *ACS Appl. Mater. Interfaces* **2017**, *9*, 38977-38983.

(2) Voogt, E. H.; Mens, A. J. M.; Gijzeman, O. L. J.; Geus, J. W. XPS Analysis of Palladium Oxide Layers and Particles. *Surf. Sci.* **1996**, *350*, 21–31.

(3) Doniach, S.; Sunjic, M. Many-Electron Singularity in X-ray Photoemission and X-ray Line Spectra from Metals. *J. Phys. C: Solid State Phys.* **1970**, *3*, 285-291.

(4) Gong, C.; McDonnell, S.; Qin, X.; Azcatl, A.; Dong, H.; Chabal, Y. J.; Cho, K.; Wallace, R. M. Realistic Metal-Graphene Contact Structures. *ACS Nano* **2014**, *8*, 642–649.

(5) Moulder, J. F.; Stickle, W. F.; Sobol, P. E.; Bomben, K. D. *Handbook of X-Ray Photoelectron Spectroscopy*; Chastain, J., Ed.; Eden Prairie, **1992**.

(6) Nan, H.; Wang, Z.; Wang, W.; Liang, Z.; Lu, Y.; Chen, Q.; He, D.; Tan, P.; Miao, F.; Wang, X.; Wang, J.; Ni, Z. Strong Photoluminescence Enhancement of MoS_2 through DefectEngineering and Oxygen Bonding. *ACS Nano* **2014**, *8*, 5738–5745.

(7) Tongay, S.; Suh, J.; Ataca, C.; Fan, W.; Luce, A.; Kang, J. S.; Liu, J.; Ko, C.; Raghunathanan, R.; Zhou, J.;Ogletree, F.; Li, J.; Grossman, J. C.; Wu, J. Defects Activated Photoluminescence in Two-Dimensional Semiconductors: Interplay between Bound, Charged and Free Excitons. *Sci. Rep.* **2013**, *3*, 2657.

(8) Pauling, L. The Nature of the Chemical Bond. *J. Am. Chem. Soc.* **1931**, *53*, 1367-1400.

(9) Luo, Y-R. In *Comprehensive Handbook of Chemical Bond Energies*; CRC Press, Taylor & Francis Group: Boca Raton, FL, 2007.

(10) Sevy, A.; Huffaker, R. F.; Morse, M. D.; Bond Dissociation Energies of Tungsten

Molecules: WC, WSi, WS, WSe, and WCl. *J. Phys. Chem. A.* **2017**, *121*, 9446-9457.

(11) Gibson, S. T.; Greene, J. P.; Berkowitz, J. A Photoionization Study of HSe and H_2Se. *J. Chem. Phys.* **1986**, *85*, 4815.

(12) Tran Khac, B. C.; Jeon, K. J.; Choi, S. T.; Kim, Y. S.; Delrio, F. W.; Chung, K. H. Laser-Induced Particle Adsorption on Atomically Thin MoS_2. *ACS Appl. Mater. Interfaces* **2016**, *8*, 2974–2984.

(13) Shi, W.; Lin, M.-L.; Tan, Q.-H.; Qiao, X.-F.; Zhang, J.; Tan, P.-H. Raman and Photoluminescence Spectra of Two-Dimensional Nanocrystallites of Monolayer WS_2 and WSe_2. *2D Mater.* **2016**, *3*, 025016.

(14) Nemanich, R. J.; Tsai, C. C.; Thompson, M. J.; Sigmon, T. W. Interference Enhanced Raman Scattering Study of the Interfacial Reaction of Pd on a-Si:H. *J. Vac. Sci. Technol.* **1981**, *19*, 685-688.

(15) Rasmussen, F. A.; Thygesen, K. S. Computational 2D Materials Database: Electronic Structure of Transition-Metal Dichalcogenides and Oxides. *J. Phys. Chem. C* **2015**, *119*, 13169–13183.

(16) Addou, R.; Wallace, R. M. Surface Analysis of WSe_2 Crystals: Spatial and Electronic Variability. *ACS Appl. Mater. Interfaces* **2016**, *8*, 26400–26406.

(17) McDonnell, S.; Addou, R.; Buie, C.; Wallace, R. M.; Hinkle, C. L. Defect Dominated Doping and Contact Resistance in MoS_2. *ACS Nano* **2014**, *8* 2880–2888.

(18) University of Texas at Dallas Cleanroom http://www.utdallas.edu/research/cleanroom/ (accessed Oct 26, 2017).

(19) Horcas, I.; Fernández, R.; Gómez-Rodríguez, J. M.; Colchero, J.; Gómez-Herrero, J.; Baro, A. M. WSXM: A Software for Scanning Probe Microscopy and a Tool for

Nanotechnology. *Rev. Sci. Instrum.* **2007**, *78*, 013705.

(20) Gong, C.; Huang, C.; Miller, J.; Cheng, L.; Hao, Y.; Cobden, D.; Kim, J.; Ruoff, R. S.; Wallace, R. M.; Cho, K.; Xu, X.; Chabal, Y. J. Metal Contacts on Physical Vapor Deposited Monolayer MoS_2. *ACS Nano* **2013**, *7*, 11350–11357.

(21) R. C. Weast, D. R. Lide, M. J. Astle, W. H. B. Selected Values of Chemical Thermodynamic Properties. In *CRC Handbook of Chemistry and Physics*; CRC Press: Boca Raton.

(22) Schmitsdorf, R. F.; Kampen, T. U.; Monch, W. Explanation of the Linear Correlation Between Barrier Heights and Ideality Factors of Real Metal-Semiconductor Contacts by Laterally Nonuniform Schottky Barriers. *J. Vac. Sci. Technol. B* **1997**, *15*, 1221-1225.

(23) Tung, R. T. Electron Transport of Inhomogeneous Schottky Barriers. *Appl. Phys. Lett.* **1991**, *58*, 2821-2823.

(24) Kim, K.; Larentis, S.; Fallahazad, B.; Lee, K.; Xue, J.; Dillen, D. C.; Corbet, C. M.; Tutuc, E. Band Alignment in WSe_2–Graphene Heterostructures. *ACS Nano*, **2015**, *9*, 4527-4532.

(25) D. K. Schroder, Semiconductor Material and Device Characterization, 3rd ed., John Wiley & Sons, Inc., NJ, USA 2006.

(26) Liu, W.; Cao, W.; Kang, J.; Banerjee, K. High–Performance Field–Effect–Transistors on Monolayer WSe_2. *ECS Trans.* **2013**, *58*, 281-285.